ADVANCED MATERIALS
www.advmat.de

Topology and Material Optimization in Ultra-Soft Magneto-Active Structures: Making Advantage of Residual Anisotropies

Carlos Perez-Garcia, Rogelio Ortigosa, Jesús Martínez-Frutos, and Daniel Garcia-Gonzalez**

Ultra-soft magnetoactive materials (stiffness <10 kPa) have transformed bioengineering and soft robotics, enabling remote actuation within soft biologically relevant environments. Despite major advances in the last decade, the complexity of their magneto-mechanical coupled behavior still hinders efficient topology and material optimization strategies for these smart structures. Two primary challenges remain: incomplete understanding and identification of the underlying physical mechanisms, and numerical limitations that restrict realistic simulation of the fully coupled problem. This work addresses these challenges by identifying and characterizing mechanical anisotropies arising from residual magnetization. In ultra-soft matrices, residual magnetization leads to microstructural rearrangements of magnetic particles, inducing mechanical anisotropy even without external fields. This anisotropy depends nonlinearly on matrix stiffness, particle properties, volume fraction, and apparent magnetization direction. These dependencies are experimentally quantified and described by a new constitutive model. The model is implemented within a computational framework that integrates these effects into advanced topology and material optimization algorithms. The framework is then used to demonstrate how accounting for these physical mechanisms enables the design of magneto-mechanical responses with improved control and functionality.

1. Introduction

In recent years, there has been a growing interest in the development of multifunctional materials and structures capable of adapting their mechanical behavior in response to external stimuli.[1–4] Among these, magnetically responsive systems have emerged as a particularly attractive class due to their ability to undergo rapid, wireless, and reversible actuation under magnetic fields. This unique combination of properties has enabled a wide range of applications across fields such as soft robotics,[5–8] biomedical devices,[9–11] active textiles or wearables,[12,13] and morphing systems.[8,14,15] In particular, magneto-active materials are especially promising in scenarios that require extreme compliance, such as biomedical interfaces or implantable devices, where the mechanical properties of the actuating system must closely match those of soft biological tissues.[11,16–18]

Despite their potential, the rational design of magneto-active structures remains a major challenge due to the complex interplay between material behavior, geometry, and actuation.[19–21] At the material level, the magneto-mechanical response is often governed by strongly nonlinear and anisotropic phenomena, including field-induced stiffening, remanent magnetization, and microstructural particle interactions.[22–24] These effects are further complicated in ultra-soft materials, where even small magnetic forces can induce significant deformations and trigger nontrivial couplings between bending, stretching, and local torques.[25,26] Structurally, the interactions between different regions of the material, mediated by long-range magnetic fields, can lead to emergent behaviors that are highly sensitive to both the geometry of the system and the relative positioning of active domains.[15,27] Moreover, reproducing real-world actuation scenarios requires taking into account the spatial and temporal characteristics of the external magnetic sources, which adds another layer of complexity to the design process.[15,22]

To address these challenges, two fundamental components are required. First, it is essential to identify and characterize the dominant magneto-mechanical deformation mechanisms that

C. Perez-Garcia, D. Garcia-Gonzalez
Department of Continuum Mechanics and Structural Analysis
Universidad Carlos III de Madrid
Avenida de la Universidad 30, Leganes 28911, Madrid, Spain
E-mail: danigarc@ing.uc3m.es1
R. Ortigosa, J. Martínez-Frutos
Multiphysics Simulation and Optimization Lab
Technical University of Cartagena
Campus Muralla del Mar, Cartagena 30202, Murcia, Spain
E-mail: jesus.martinez@upct.es

The ORCID identification number(s) for the author(s) of this article can be found under https://doi.org/10.1002/adma.202518489

DOI: 10.1002/adma.202518489

govern the behavior of the material, particularly in the ultra-soft regime where standard assumptions often break down.[28–31] Second, robust computational tools must be developed to simulate and optimize the performance of these materials under realistic conditions, accounting for nonlinearities, anisotropy, and the coupling between magnetic and mechanical fields.[20,32,33]

In this work, we address these open challenges by introducing a combined experimental and computational framework tailored to the design of ultra-soft magneto-active structures. We begin by identifying a previously overlooked deformation mechanism: the emergence of residual mechanical anisotropy in hard-magnetic magnetorheological elastomers (hMREs) resulting from remanent magnetization, even in the absence of external fields. We then develop an invariant-based neural network constitutive model that captures this anisotropy and incorporates it into a variational formulation compatible with finite element analysis. Leveraging this model, we implement a physics-informed topology optimization platform capable of designing programmable structures with complex actuation responses. Our approach integrates material characterization, constitutive modeling, field resolution (including vacuum effects) and inverse design within a unified pipeline. We validate the framework through a series of experimental studies and demonstrate that neglecting remanence-induced anisotropy can lead not only to quantitative inaccuracies but also to qualitative errors such as mode switching. Finally, we show that our framework enables the design of active components that achieve precise and programmable deformations, even in regimes where classical design strategies fail. These contributions provide a foundation for the next generation of magnetically actuated soft systems and highlight the critical role of material anisotropy in shaping their mechanical performance.

2. Results

2.1. Residual Mechanical Anisotropy Originates From the Interplay Between Matrix Stiffness and Particle Remanent Magnetization

Previous work on magnetorheological elastomers (MREs) has shown the possibility to introduce anisotropic distributions of magnetic particles by applying an external magnetic field during the curing process.[34–37] The magnetic forces experienced by the particles within the pre-cured elastomer, i.e., in liquid phase, lead to the formation of particles chain-like structures along the field direction.[38,39] In the absence of such a field, the particles remain isotropically distributed after matrix solidification.[40,41] When these MREs present hard-magnetic particles (hMREs), the application of a strong magnetic pulse post-curing can magnetically saturate the particles, introducing remanent magnetization.[36] Several previous works have demonstrated strong anisotropies in magnetic properties, but an isotropic mechanical behavior in the absence of externally applied magnetic fields.[41–44] This assumption has remained, with most experimental and theoretical studies overlooking the possibility of remanent magnetization inducing mechanical anisotropy. Although this effect is negligible in MREs with stiff polymer matrices, it can lead to significant mechanical anisotropies in ultra-soft hMREs.

Figure 1A schematically illustrates the formation of microstructural patterns in hMREs following sample magnetization. Initially, magnetic particles are randomly and isotropically distributed within the cured sample. Then, the sample is exposed to a fast magnetic pulse (typically 2–5 T over a few ms), which drives the particles to magnetic saturation. The resulting remanent magnetization generates interparticle forces, both attractive and repulsive, that act to reorient and align the particles into chain-like structures along the direction of the applied magnetic field. These magnetic interaction forces are resisted by the passive elasticity of the surrounding polymer matrix, and the system eventually reaches a mechanical equilibrium in the absence of any external magnetic field. The resulting microstructure and the associated anisotropy depend on several key manufacturing parameters. The stiffness of the matrix is particularly influential, with softer materials allowing for greater particle displacement, needed to reach the internal mechanical stresses to counterbalance these interactions. Similarly, the magnitude of the remanent magnetization affects the strength of interparticle forces: greater remanence leads to stronger interactions and, consequently, larger relative displacements. The volume fraction of magnetic particles also plays a dual role: higher concentrations reduce interparticle distance and enhance magnetic interactions but simultaneously increase the composite stiffness, limiting local deformations. Beyond the percolation threshold, excessive particle loading can lead to aggregation, which may diminish the effectiveness of magnetic interactions. Lastly, the direction of magnetization governs the orientation of the particle chains, ultimately determining the anisotropic mechanical response of the material. In this work, we explore how combinations of matrix stiffness, particle volume fraction, remanent magnetization, and magnetization direction affect the emergence and characteristics of mechanical anisotropy in hMREs under zero external magnetic actuation (see Figure 1B).

We characterize this magnetically induced mechanical anisotropy in soft hMREs through uniaxial tensile tests on rectangular non-magnetized (virgin) and magnetized samples (Figure 1A). We consider polymeric matrix materials with different stiffness, i.e., Dowsil CY52-276 (Dow, ≈3 kPa) and Sylgard 184 (Syl, ≈2 MPa). Different volume fractions of micron-sized Nd particles (20%, 30%, and 40%) are incorporated into the matrix. For additional details on the fabrication and testing procedures, see the Materials and Methods section. To assess the mechanical anisotropy induced by premagnetization, the samples are magnetized along the three different directions: 0°, 45°, and 90°, as illustrated in Figure 1B.

Figure 1C shows the true stress–stretch curves from uniaxial tensile tests for samples with the ultra-soft Dow matrix, both in the virgin state and combined with 30% volume fraction of Nd particles. The inclusion of non-magnetized particles, with stiffness on the order of GPa, increases the stiffness of the hMRE without introducing significant nonlinear effects. The premagnetization of the samples, as illustrated in Figure 1B, induces a remanent magnetization in the material in those specific directions. This remanence generates magnetic interactions between the embedded particles, resulting in the apparent stiffening of the hMRE. Furthermore, the material exhibits mechanical anisotropy following the pre-magnetization direction. Maximum stiffness occurs when the remanent magnetization orientation

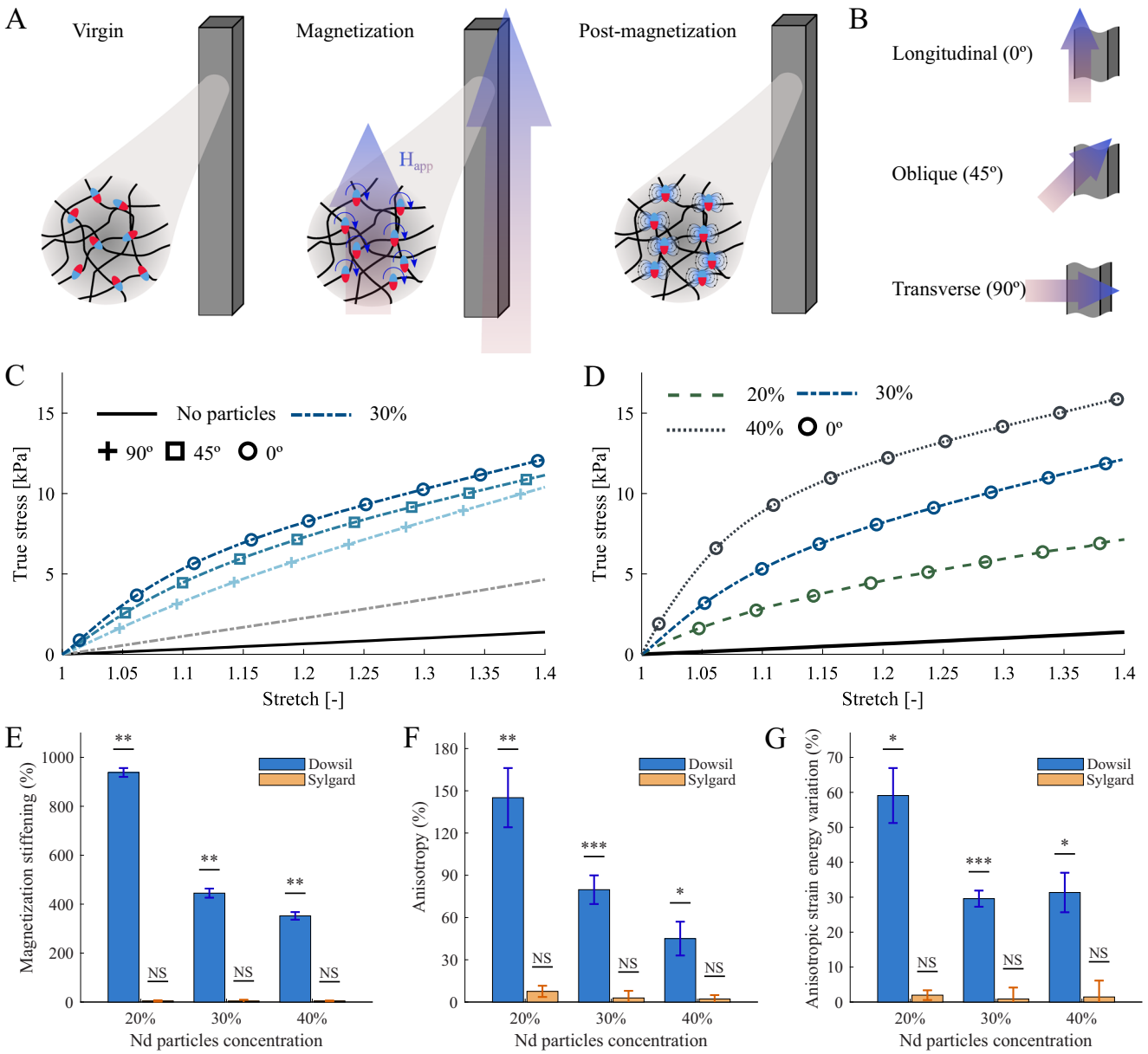

Figure 1. Magnetically induced anisotropy on the mechanical response of hMREs. A) Pre-magnetization of hMRE samples by subjecting them to a strong external magnetic field. During this process, the Nd particles align with the external field, forming chains and exhibiting a remanent magnetic field. B) Pre-magnetization directions considered in this work. C,D) Material characterization and anisotropy analysis of hMREs based on ultra-soft elastomeric matrix. Panel (C) presents the true stress-stretch curves under uniaxial tension, showing the stiffening phenomena due to the inclusion of Nd particles, and the mechanical anisotropy depending on the pre-magnetization orientation. Panel (D) demonstrates, via true stress–stretch curves, the linear relationship between Nd particles concentration and material stiffening in addition to the nonlinear material response. E–G) Analysis of the effect on material stiffening and induced anisotropy under different particle concentrations for Dowil (Dow) and Sylgard (Syl) matrices. Panel (E) shows stiffness enhancement due to material pre-magnetization for the ultra-soft Dow matrix, and no significant stiffening for the Syl matrix for deformations up to 5%. Panel (F) demonstrates the induced anisotropy of the ultra-soft Dow matrix and the negligible anisotropy of the Syl matrix for deformations up to 5%. Panel (G) shows variations in strain energy due to anisotropy, illustrating how the anisotropy derived from pre-magnetization decreases under large deformations. This confirms that particle–particle interactions weaken with strain, resulting in a more compliant material and reduced stiffness differences. Data are presented as relative increment of each variable ± SEM. Comparisons were performed by statistical *t*-test with multiple comparisons, * $p \leq 0.05$, ** $p \leq 0.01$, *** $p \leq 0.001$.

($\mu_0 H_r$) is parallel to the applied force; i.e., the stiffness increases as the angle between these orientations decreases.

The volume fraction of Nd particles plays a key role in determining the mechanical response of hMREs. In Figure 1D, we present the results of the tensile test for samples with three different particle concentrations (20%, 30%, and 40%), all pre-magnetized along the same orientation (0°), which yields the stiffest response. Within the small-strain regime (up to approximately ≈5–10%), a linear increase in material stiffness is observed as the particle concentration increases. At larger strains, the non-linear behavior of the elastomer becomes more significant as a result of the reduced interparticle distances at higher concentrations of particles. In these cases, the material initially exhibits a steeper response at low strains, dominated by magnetic interactions between Nd particles, followed by a softer response at higher strains where matrix stiffness begins to dominate the mechanical behavior. The complete set of characterization tests and their quantification are provided in Supporting Information (Figures S1 and S2, and Tables S2– S4, Supporting Information).

The influence of the magnetically induced anisotropy, depending on the matrix stiffness and particle concentration, is quantified in Figure 1E–G. Figure 1E analyzes the magnetization stiffening, defined as the ratio between the stiffness under small strains (up to 5%) of the non-magnetized material and that of the magnetized material (0°, i.e., magnetization aligned with loading direction). For the ultra-soft matrix (Dow), we observe a clear decrease in magnetic stiffening with particle concentration (c) when approaching the percolation threshold. The most pronounced effect is found at c = 20%, where the magnetized sample presents a stiffening of almost 1000% with respect to the non-magnetized. For the stiffer matrix (Syl), the stiffening effect is negligible. Figure 1F evaluates the mechanical anisotropy of the samples due to residual magnetization. This is defined comparing the stiffness under small strain between the samples magnetized at 0° and 90° with respect to the loading direction. An inverse relationship was found between the concentration of particles (c) and the magnitude of anisotropy, which is also attributed to the percolation threshold. The magnetically induced mechanical anisotropy is evident for all cases when using the soft matrix (Dow) but negligible when using the stiffer one (Syl). The highest anisotropy occurs at the lowest concentration (c = 20%), with an anisotropic variation of nearly 150%. Finally, Figure 1G analyzes the increase in strain energy between samples magnetized parallel (0°) and perpendicular to the loading direction. These results show the reduced contribution of magnetic interactions under large deformations, as the interparticle distance increases under large deformations resulting in weaker magnetic interactions and a more compliant material response. The hMRE samples with the softer matrix (Dow) show a maximum relative increase in strain energy of around 60% due to residual magnetization. By contrast, the stiffer matrix (Syl) exhibits no significant stiffening post-premagnetization. These results illustrate the fundamental importance of matrix compliance in magneto-mechanical coupling and the need for considering the anisotropic behavior in hMREs arising from residual magnetization. To provide direct microstructural evidence of this mechanism, combined SEM and optical microscopy images of cross-sections of magnetized and non-magnetized Dowsil-based hMRE samples are included in Figure S3 (Supporting Information), confirming the transition from a random particle distribution to chain-like arrangements aligned with the remanent field. The stability of the magnetically induced anisotropy under repeated loading was verified through cyclic tensile tests on Dowsil- and Sylgard-based hMREs with different residual magnetization orientations, confirming that the remanent field-induced anisotropy originated in the ultra-soft hMREs remains stable over multiple cycles (see Figure S4 and Table S5, Supporting Information).

2.2. Invariant-Based NN Algorithm to Describe Mechanical Anisotropy Originated From Residual Magnetization

As discussed in the previous section and illustrated in Figure 1, the mechanical response of ultra-soft hMREs is strongly influenced by microstructural particle interactions, even in the absence of externally applied magnetic fields. These interactions, governed by the remanent magnetization of the embedded particles, give rise to residual mechanical anisotropy that persists under stress-free conditions. Notably, this remanence-induced anisotropy manifests as directional variations in stiffness, fundamentally altering the deformation behavior of the material. These experimental observations underscore the need for advanced computational tools to support the design of magnetically responsive structures. In particular, the optimal design of MRE-based devices requires numerical frameworks that not only ensure stability and robustness, but also incorporate physically accurate constitutive models. The complex and nonlinear coupling between magnetic and mechanical fields in soft hMREs calls for constitutive formulations capable of capturing these intertwined effects.

To address this challenge, we propose a constitutive framework based on a variational formulation of the total energy, which incorporates isotropic, anisotropic, magnetic, and vacuum contributions. This formulation is expressed in terms of invariants, and serves as the foundation for a data-driven identification of the magneto-mechanical response using a neural network (NN) architecture (**Figure 2A**). The complete formulation is based on invariants, defined as:

$$I_1 = \boldsymbol{F} : \boldsymbol{F}; \qquad I_2 = \mathrm{Cof}\boldsymbol{F} : \mathrm{Cof}\boldsymbol{F}; \qquad I_3 = \det \boldsymbol{F};$$
$$I_4 = \boldsymbol{F}\boldsymbol{H}_r \cdot \boldsymbol{F}\boldsymbol{H}_r; \qquad I_6 = \mathrm{Cof}\boldsymbol{F}\boldsymbol{H}_r \cdot \mathrm{Cof}\boldsymbol{F}\boldsymbol{H}_r; \tag{1}$$
$$I_5^e = \boldsymbol{H} \cdot \boldsymbol{C}^{-1} \cdot \boldsymbol{H} \qquad I_5^{er} = \boldsymbol{H} \cdot \boldsymbol{C}^{1/2} \cdot \boldsymbol{H}_r$$

where $\boldsymbol{F}$ is the deformation gradient, $\boldsymbol{H}$ is the magnetic field, $\boldsymbol{H}_r$ is the remanent magnetic field (a material and design parameter), and $\boldsymbol{C} = \boldsymbol{F}^T\boldsymbol{F}$. The total potential energy is expressed as:

$$\Psi(\boldsymbol{F}, \boldsymbol{H}) = \Psi_{\mathrm{iso}}(\boldsymbol{F}) + \Psi_{\mathrm{ani}}(\boldsymbol{F}) + \Psi_{\mathrm{mag}}(\boldsymbol{F}, \boldsymbol{H}) + \Psi_{\mathrm{Maxw}}(\boldsymbol{F}, \boldsymbol{H}) \tag{2}$$

where $\Psi_{\mathrm{mag}}(\boldsymbol{F}, \boldsymbol{H}) = -\frac{\mu_0}{2}\chi I_5 + \mu_0[1+\chi] I_5^{er}$ and $\Psi_{\mathrm{Maxw}}(\boldsymbol{F}, \boldsymbol{H}) = -\frac{\mu_0}{2} I_5$ are the magnetization and vacuum terms, respectively, with μ_0 being the magnetic permeability in vacuum and χ the magnetic susceptibility of the MRE. It is worth noting that the proposed formulation is structurally consistent with earlier theoretical models, such as those introduced by Mukherjee et al.[45,46] and Danas and Reis,[47] in which a similar coupling term was used to represent magnetic-field-induced anisotropy. In contrast

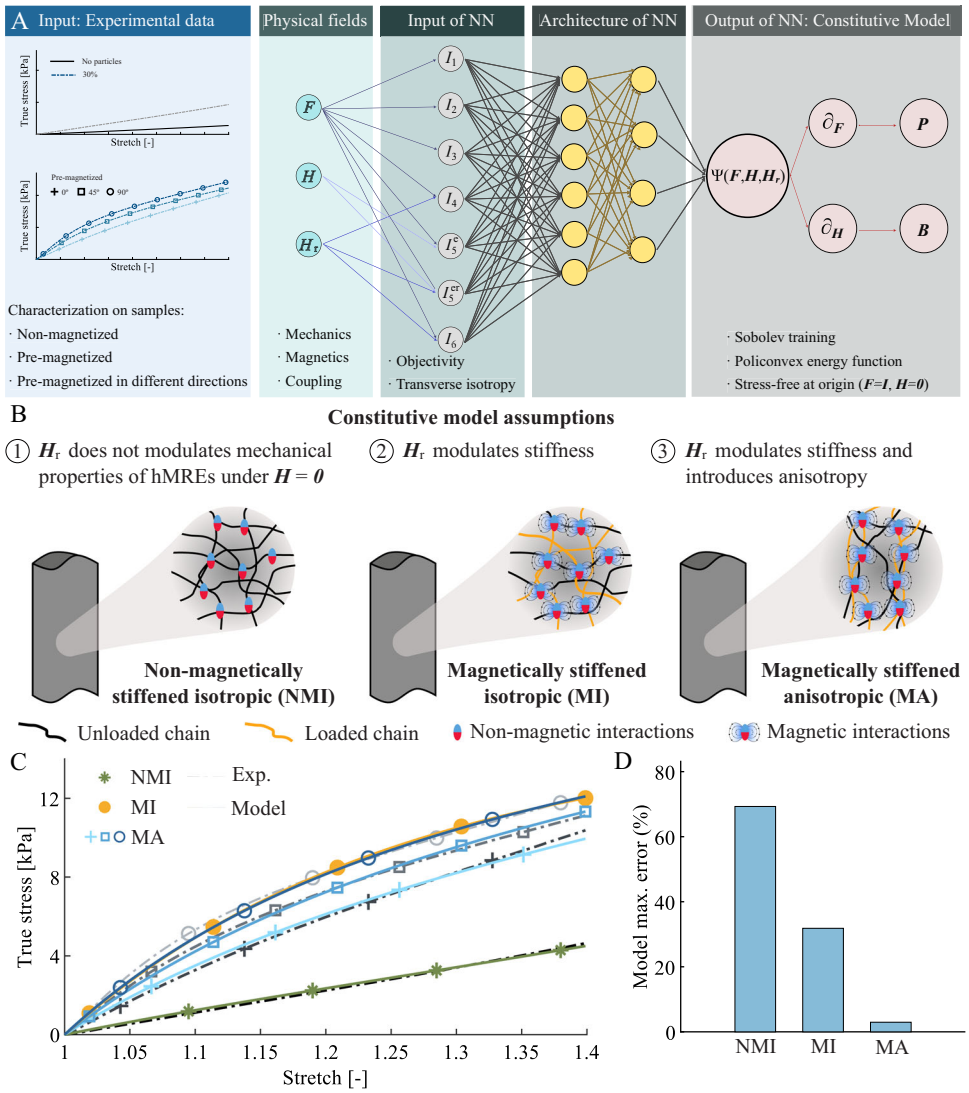

Figure 2. Constitutive modeling framework for capturing residual anisotropy in ultra-soft hMREs via an invariant-based NN. A) Schematic overview of the data-driven constitutive modeling strategy. Experimental data are collected for different magnetization states (non-magnetized, pre-magnetized, and directionally pre-magnetized). These data are used to calibrate an invariant-based NN that maps physically consistent inputs to the total energy potential. The architecture enforces material frame indifference, transverse anisotropy, Sobolev-type training, polyconvexity, and stress-free conditions in the undeformed reference state. B) Conceptual assumptions underlying three constitutive modeling approaches: 1) the non-magnetically stiffened isotropic (NMI) model assumes $\boldsymbol{H}_r$ has no effect under zero field; 2) the magnetically stiffened isotropic (MI) model includes stiffening due to remanent magnetization; and 3) the magnetically stiffened anisotropic (MA) model additionally accounts for the anisotropy introduced by directional magnetic interactions. C) Validation of the three constitutive models by comparing predicted and experimental true stress–stretch curves under uniaxial loading for ultra-soft hMRE samples (Dow). D) Maximum relative error for each constitutive assumption with respect to experimental data. Models neglecting magnetic anisotropy exhibit significantly higher predictive errors, with the MA model reducing the error below 3%.

to those studies, which focused on stiffer polymers and moderate deformations, the present work extends the formulation to the ultra-soft regime, where remanence-induced anisotropy becomes a dominant mechanism. This necessitates a re-evaluation of the constitutive assumptions and a new experimental calibration of the material parameters to capture the nonlinear magneto-mechanical interactions characteristic of ultra-soft hMREs.

This structure is used to build and constrain a NN model that approximates the total energy density Ψ in a physically consistent manner. Although an explicit analytical formulation is provided for the specific ultra-soft hMREs studied here, the invariant-based neural network implementation grants the framework full generality, allowing users to derive constitutive models directly from mechanical characterization data for other magneto-active materials exhibiting different coupling behaviors. To this end, we construct a Sobolev-type NN, trained not only to fit energy values but also their derivatives with respect to the deformation gradient $\boldsymbol{F}$ and magnetic field $\boldsymbol{H}$, ensuring accurate prediction of stress and magnetic induction. This is crucial for their proper integration into magneto-mechanical FE simulations and optimization processes.

The neural network takes as input the invariant set $I_1, I_2, I_3, I_4, I_5, I_5^{er}, I_6$, and outputs the scalar energy potential Ψ (Figure 2A). This invariant-based formulation guarantees material frame indifference by construction, as it eliminates any explicit dependence on directional tensor quantities. The inclusion of I_4 and I_6 enables the model to naturally capture transverse anisotropy induced by remanent magnetization. To ensure polyconvexity, and thus the numerical stability of the resulting constitutive law, we enforce specific architectural constraints: i) all network weights are constrained to be non-negative, ensuring convexity with respect to the input invariants; and ii) activation functions are chosen to be monotonically increasing, preserving convexity through their composition. Additionally, the magnetized hMRE is treated as the undeformed reference configuration, meaning that the material is assumed to be stress-free when $\boldsymbol{F} = \boldsymbol{I}$ and $\boldsymbol{H} = \boldsymbol{0}$. This condition is enforced during training by penalizing any residual stresses or magnetic forces at the origin.

The network is trained using a custom loss function that incorporates both energy values and their first derivatives with respect to $\boldsymbol{F}$ and $\boldsymbol{H}$, providing accurate predictions of stress and magnetic induction. This Sobolev-type training strategy enhances generalization and ensures the model adheres to the governing physical principles across a broad range of deformations and field conditions. Although the framework allows for general magneto-mechanical coupling, in this work we focus on hMREs based on Nd-based microparticles, which exhibit magnetic remanence but very low magnetic susceptibility. This enables direct experimental characterization of magnetic parameters and justifies fixing the magnetic component during training. Consequently, the network learns only the mechanical response, including the effects of remanence-induced anisotropy, while the magnetic contribution remains constant across samples. This simplification, grounded in experimental observations, facilitates model calibration and improves robustness for the inverse design of magnetically actuated structures.

To demonstrate the importance of capturing remanence-induced effects in soft hMREs, we compare three constitutive model assumptions (Figure 2B). The first, referred to as "non-magnetically stiffened isotropic (NMI)," reflects the most common approach found in the literature. This model is calibrated using data from non-magnetized samples (Figure 2C) and does not account for the stiffening or anisotropy associated with remanent magnetization. The second model, "magnetically stiffened isotropic (MI)," incorporates the additional stiffness resulting from residual magnetic interactions but assumes the response remains isotropic. This model is calibrated against samples magnetized along their longitudinal direction (0°). Finally, the "magnetically stiffened anisotropic (MA)" model includes both the stiffening and the anisotropic effects induced by remanent magnetization, as captured experimentally. This complete formulation introduces the additional energy term Ψ_{ani} to represent directional mechanical reinforcement. Figure 2C compares the predictive performance of the three models for ultra-soft hMREs under uniaxial tension (see Figure S5, Supporting Information, for results with stiffer matrices). The NMI model captures only the baseline stiffening due to particle inclusion, failing to reproduce the enhanced response caused by magnetic interactions. As a result, it exhibits predictive errors of up to 70% (Figure 2D). The MI model successfully reproduces the magnetically induced stiffening observed in pre-magnetized samples by accounting for inter-particle interactions and the effects of remanent fields. However, it neglects anisotropy and therefore underperforms in samples with strong directional response, with errors exceeding 30%. In contrast, the MA model captures both stiffening and anisotropic effects under complex deformation states, reducing the maximum prediction error to below 3%. These results highlight the critical role of inter-particle magnetic interactions in governing the mechanical response of soft hMREs and demonstrate the necessity of anisotropic constitutive models for accurate prediction. The constitutive model was calibrated using experimental data from non-magnetized and pre-magnetized samples (with and without $\boldsymbol{H}_r$) under zero external field, and is subsequently validated, without additional fitting, against the actuation experiments shown in next sections, demonstrating excellent predictive accuracy under realistic magnetic loading conditions. Overall, the framework presented here provides a reliable and efficient tool for simulating the magneto-mechanical behavior of hMREs in design scenarios where residual magnetization plays a key functional role.

2.3. Experimental Limitations of Conventional Programming Strategies in Ultra-Soft hMREs

A widely adopted strategy to program the actuation response of hMRE components is based on a straightforward fabrication protocol: the material is molded into a specific geometry, then deformed into a desired shape and magnetized under a strong external field.[36,48] This process introduces a residual magnetization pattern aligned with the imposed deformation (**Figure 3A**), such that, upon re-actuation, the structure reproduces the target configuration (Figure 3B). This principle has been successfully used in hMRE systems with relatively high stiffness, particularly in slender elements actuated primarily through bending, where the mechanical response closely follows the magnetization pattern encoded during fabrication.[48] However, this approach fails when applied to ultra-soft hMREs. As shown in Figure 3C, two samples fabricated using the same protocol but with different stiffness levels exhibit drastically different responses under actuation. In the stiffer sample (Syl), the imposed deformation is recovered with high fidelity, validating the assumptions of traditional design workflows. In contrast, the ultra-soft sample (Dow) displays a deformation that deviates significantly from the programmed shape, despite having the same residual magnetization field distribution. This failure is not due to fabrication imprecision, but rather to a breakdown of the assumptions underlying the conventional paradigm.

The divergence observed in the soft sample reveals the presence of additional physical mechanisms that dominate in the ultra-soft regime. These include large strains involving both bending and membrane stretching, important gravitational body forces, microstructural torques that reorient the remanent magnetization under external loading, and mechanically induced anisotropy resulting from magnetized particle interactions, even in the absence of external fields. These nonlinear and coupled effects fundamentally alter the actuation behavior, making it impossible to rely solely on magnetization-aligned shape

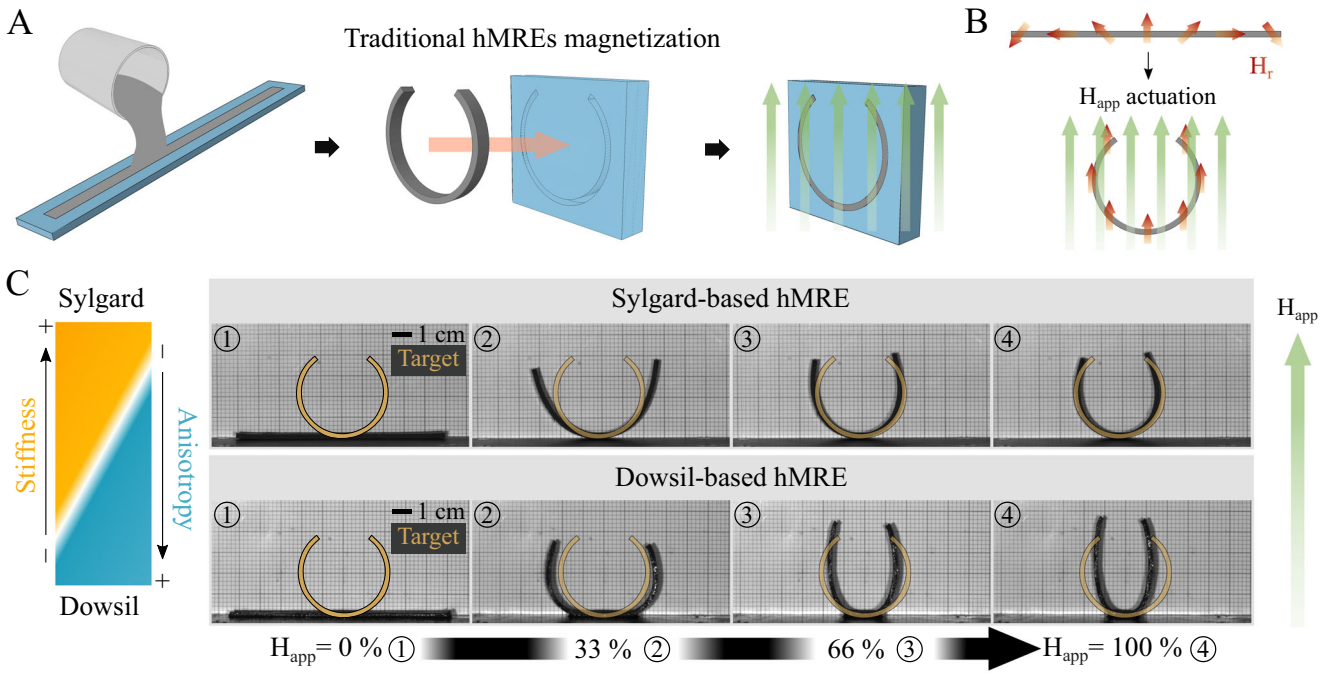

Figure 3. Experimental validation of traditional programming strategies for hMRE-based actuators. A) Schematic of the conventional magnetization process used to program hMRE structures. The actuator is fabricated, inserted into a custom mold that imposes a desired deformed shape, and then exposed to a strong magnetic pulse. This process imprints a residual magnetization field aligned with the imposed geometry. B) Example of a programmed residual magnetization distribution and its expected magneto-mechanical response under an externally applied magnetic field. C) Experimental actuation of beam-shaped hMREs made from two different matrix materials: Sylgard (top row) and Dowsil (bottom row). The stiff Sylgard-based sample, which exhibits low remanence-induced anisotropy, deforms as intended and follows the programmed shape. The ultra-soft Dowsil-based sample, characterized by high anisotropy, fails to reproduce the target configuration despite undergoing the same magnetization protocol. These results highlight the limitations of traditional shape-encoded programming approaches in soft hMRE systems.

programming. These experimental observations underscore the need for a new generation of computational tools capable of guiding the design of soft hMRE-based systems. In particular, the programming of magnetically actuated responses can no longer be approached as a purely geometric inverse problem. Instead, it must account for the full spectrum of governing mechanisms: geometric and material nonlinearities, field-induced anisotropy, remanent-field dynamics, and the coupled magneto-mechanical response of the system.

2.4. Designing Platform to Program Magneto-Mechanical Actuation in Ultra-Soft hMREs

The experimental results discussed in the previous section reveal the limitations of conventional programming strategies when applied to ultra-soft hMREs. Overcoming this challenge requires a fundamentally different strategy: one that integrates the underlying physics of the material and the constraints of the fabrication process into a unified design methodology. To address this challenge, we present a computational platform that integrates the invariant-based constitutive framework developed in the previous section within a topology and multimaterial optimization setting (**Figure** 4A). This platform enables the design of ultra-soft structures with programmable magneto-mechanical responses tailored to external magnetic stimuli. It provides a robust foundation for optimizing not only material distribution and residual magnetization, but also fabrication-aware pre-magnetization strategies. The design process consists of three main stages:

i) Material calibration from experimental input: The platform begins by processing material characterization data for the magnetically responsive elastomers of interest. These data are used to calibrate invariant-based neural network constitutive models that accurately reproduce the nonlinear, anisotropic, and remanent-dependent behavior of the materials.
ii) Specification of geometric and magnetic constraints: The user defines the design domain, fabrication limitations (e.g., resolution, printable zones), and characteristics of the external actuation field, including magnitude, direction, and spatial distribution.
iii) Target actuation definition and inverse design: A desired set of deformations or functionalities under magnetic loading is provided as the design goal. The platform then solves the inverse problem using a FEM solver coupled to a topology optimization engine that leverages the calibrated constitutive laws.

In this work, the remanent magnetic field H_r is treated as an experimentally measurable property rather than as the result of a fully dissipative magnetization process. Although such dissipative formulations have been proposed in previous studies

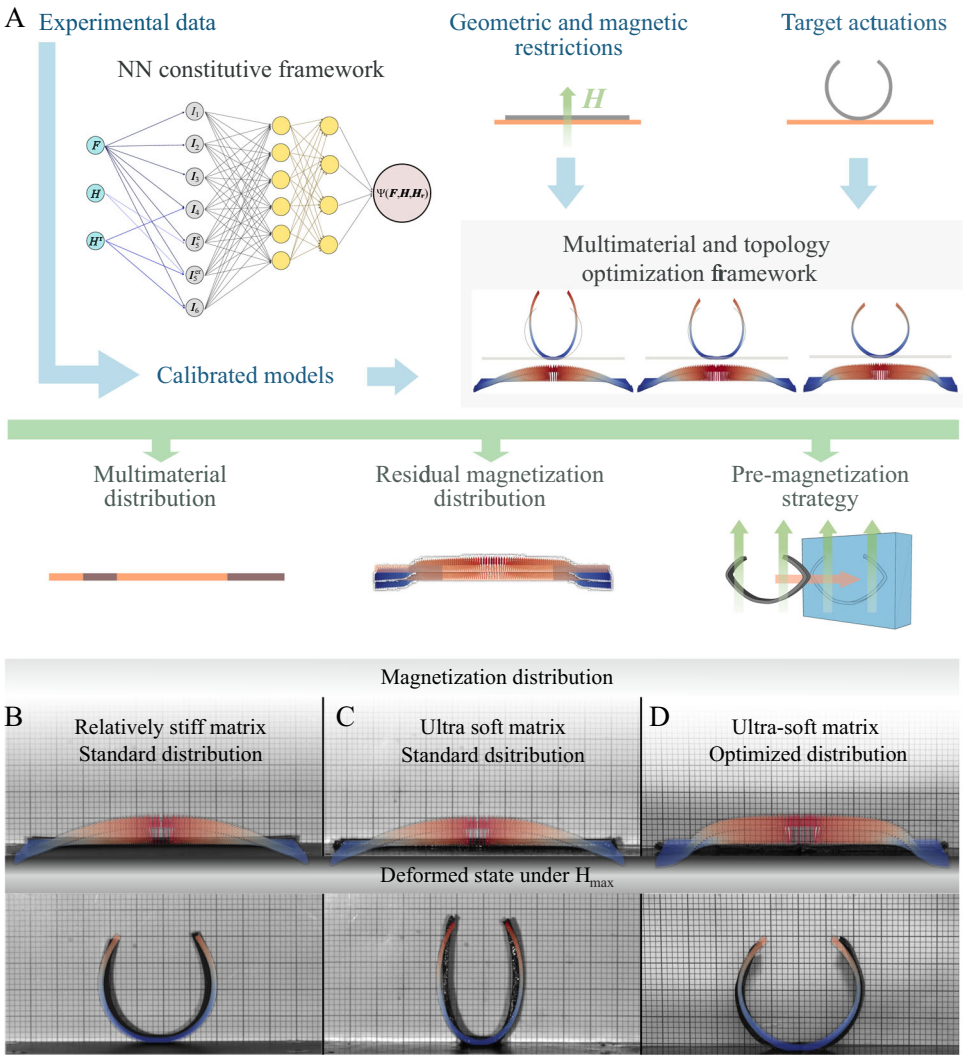

Figure 4. Computational design framework and validation for programmable magneto-mechanical actuation in ultra-soft hMREs. A) Overview of the integrated design platform. The pipeline starts with three inputs: i) experimentally calibrated constitutive models obtained from the invariant-based NN framework, ii) geometric and magnetic constraints, and (iii) target actuation profiles. These inputs are processed by a multimaterial and topology optimization framework, which outputs: 1) the spatial distribution of active and passive materials, 2) the optimized residual magnetization profile, and 3) the required pre-magnetization protocol for fabrication. B) Comparison between simulation and experiment for a stiff hMRE sample (Sylgard), actuated using a residual magnetization pattern obtained by applying a magnetic field in a pre-deformed C-shaped configuration. The programmed shape is successfully recovered. C) Equivalent comparison for a soft hMRE sample (Dowsil), using the same magnetization pattern as in (B). The target deformation is not achieved, revealing the failure of the traditional pre-deformation strategy in soft materials. D) Simulation and experimental results for the Dowsil sample using the residual magnetization distribution optimized by the proposed framework. The target C-shaped deformation is accurately recovered under magnetic actuation.

(e.g., refs. [45, 46]), their implementation requires detailed knowledge of the magnetization history and boundary conditions. Here, H_r is defined based on experimental calibration and optimized through its orientation angles (θ, ϕ) within the inverse design problem, providing a computationally efficient and experimentally grounded alternative for the ultra-soft systems considered. The remanent magnetic field H_r can be interpreted as an internal prestress field analogous to the residual stresses generated in additive manufacturing or biological growth processes, as it represents a stored internal state that modifies the stress-free reference configuration of the material.[49,50] As a result, the platform generates a fully programmable actuator design including: 1) the spatial layout of passive and active materials; 2) the optimized distribution of residual magnetization, which directly guides fabrication using additive manufacturing techniques such as direct ink writing (DIW); and 3) for molding-based fabrication, a pre-magnetization protocol that prescribes the deformed configuration required during magnetization to encode the desired residual field. By embedding the relevant physics from the outset and coupling them with the inverse design process, this platform enables the rational design of soft robotic components that exploit the full complexity of magnetically induced actuation in ultra-soft, anisotropic hMREs. It bridges the gap between experimental characterization, constitutive modeling, and application-

driven performance, opening new avenues for programmable soft matter systems.

To assess the effectiveness of the proposed computational platform, we compare simulated and experimental magneto-mechanical responses under different programming strategies and material stiffnesses (Figure 4B–D). In a first validation case, a C-shaped pre-deformation is imposed during magnetization, producing a residual magnetization pattern aligned with the curved configuration. When this profile is applied to a stiff hMRE (Sylgard), the sample successfully recovers the intended shape under external magnetic loading (Figure 4B), consistent with the assumptions of traditional design approaches. The experimental and simulated deformations show good agreement, confirming that in stiff systems, geometric programming through pre-deformation remains a viable strategy. In contrast, when the same magnetization pattern is applied to a soft hMRE (Dowsil), the resulting simulated deformation, as experimentally observed, deviates significantly from the target configuration (Figure 4C). This mismatch illustrates the failure of conventional programming in ultra-soft materials, where the magnetically induced anisotropy and remanent-field dynamics become dominant. However, when the residual magnetization is computed using the proposed topology optimization framework, the actuation response closely matches the target shape. This result reflects the framework's ability to explicitly account for the coupled magneto-mechanical physics of the system (Figure 4D). More examples of topology optimization on beam structures are shown in Figures S6 and S7 (Supporting Information). These results demonstrate the capacity of the platform to design magnetically driven deformations in ultra-soft hMREs that cannot be achieved through intuition or classical fabrication protocols alone.

Beyond inverse design for optimizing residual magnetization in homogeneous samples, the computational platform developed here also supports multimaterial optimization and programmable actuation in geometrically complex structures. This is critical for real-world applications, where passive and active materials must be distributed non-uniformly to balance actuation performance, structural integrity, and fabrication feasibility. To demonstrate this, we consider a representative design problem involving a soft circular actuator composed of multiple subdomains with distinct material properties (**Figure 5**A). Given the geometry, a target deformation, and a library of experimentally calibrated constitutive models (including both passive elastomers and magnetically active hMREs), the framework computes the optimal distribution of materials and residual magnetization that reproduces the desired actuation response. Figure 5B,C shows the outcome of the inverse design process for this problem, including the target shape, the numerical simulation of the optimized design under magnetic loading, and the corresponding experimental validation. The results confirm that the platform successfully captures the desired deformation with high fidelity. The differences observed in the central region of the experimental configuration arise from the presence of a small cylindrical support used to hold the specimen during actuation, which locally limits the achievable curvature. The optimization algorithm aims to reproduce the mathematically prescribed target deformation as closely as possible, given the material properties and boundary conditions, and the small discrepancies observed reflect these physical constraints rather than a loss of predictive accuracy. Figure 5D illustrates the same design scenario shown in Figure 5B, but under modified loading conditions that neglect gravitational forces. This setup mimics near-neutral buoyancy environments such as underwater applications, allowing the assessment of how actuation performance and deformation modes are affected when gravity is no longer a dominant factor. Other examples with more intricate geometries and material combinations are provided in the Supporting Information (Figures S8–S10, Supporting Information).

These results highlight the flexibility and robustness of the framework, which exploits spatial variations in stiffness and magnetic anisotropy to guide deformation in a highly programmable manner, achieving actuation profiles that would be difficult to realize using conventional heuristic strategies. To further demonstrate the generality of the proposed density-based formulation, which inherently enables topological changes through the creation of voids and active domains, an additional example is provided in the Supporting Information (Figure S11, Supporting Information). This example illustrates the optimization of a more complex actuator geometry, where the algorithm simultaneously determines the spatial distribution of material, voids, and magnetized regions, confirming the framework's capability to address topology optimization problems.

2.5. Full-Physics Optimization is Essential to Accurately Design Anisotropic hMRE Structures

The design of magnetically actuated structures based on ultra-soft hMREs requires numerical tools that accurately capture all relevant physical phenomena across scales. In this context, the previously introduced design platform, built upon a constitutive model capable of encoding remanence-induced anisotropy and a full-field magneto-mechanical formulation, is essential to generate reliable actuation responses. **Figure 6** illustrates how incomplete physical modeling, particularly at the constitutive level, can lead to drastically inaccurate or qualitatively incorrect results in the inverse design of hMRE-based devices.

In Figure 6A,B, we compare the optimized actuation response for two geometries using two different material models: one that considers only isotropic magnetically induced stiffening (MI), and one that includes both stiffening and directional anisotropy (MA) (see Figure 2). In both examples, the design goal is to recover a prescribed target shape under magnetic actuation. The optimization is carried out using the same target, boundary conditions, and applied field in both cases. For the beam-shaped geometry in Figure 6A, the MI model fails to reproduce the desired shape, leading to a deformation mode that deviates qualitatively from the target. In contrast, the MA model successfully captures the intended actuation through a magnetization profile that leverages anisotropic effects to direct the deformation. This failure of the MI model is not a mere quantitative error, but it reveals a mode-switching behavior driven by the underlying constitutive assumptions. A similar phenomenon is observed in the shell-like geometry of Figure 6B, where the MI-based design yields a qualitatively different actuation mode compared to both the MA model and the target. These results demonstrate that remanence-induced anisotropy is not a secondary effect, but a primary design variable that must be explicitly modeled for

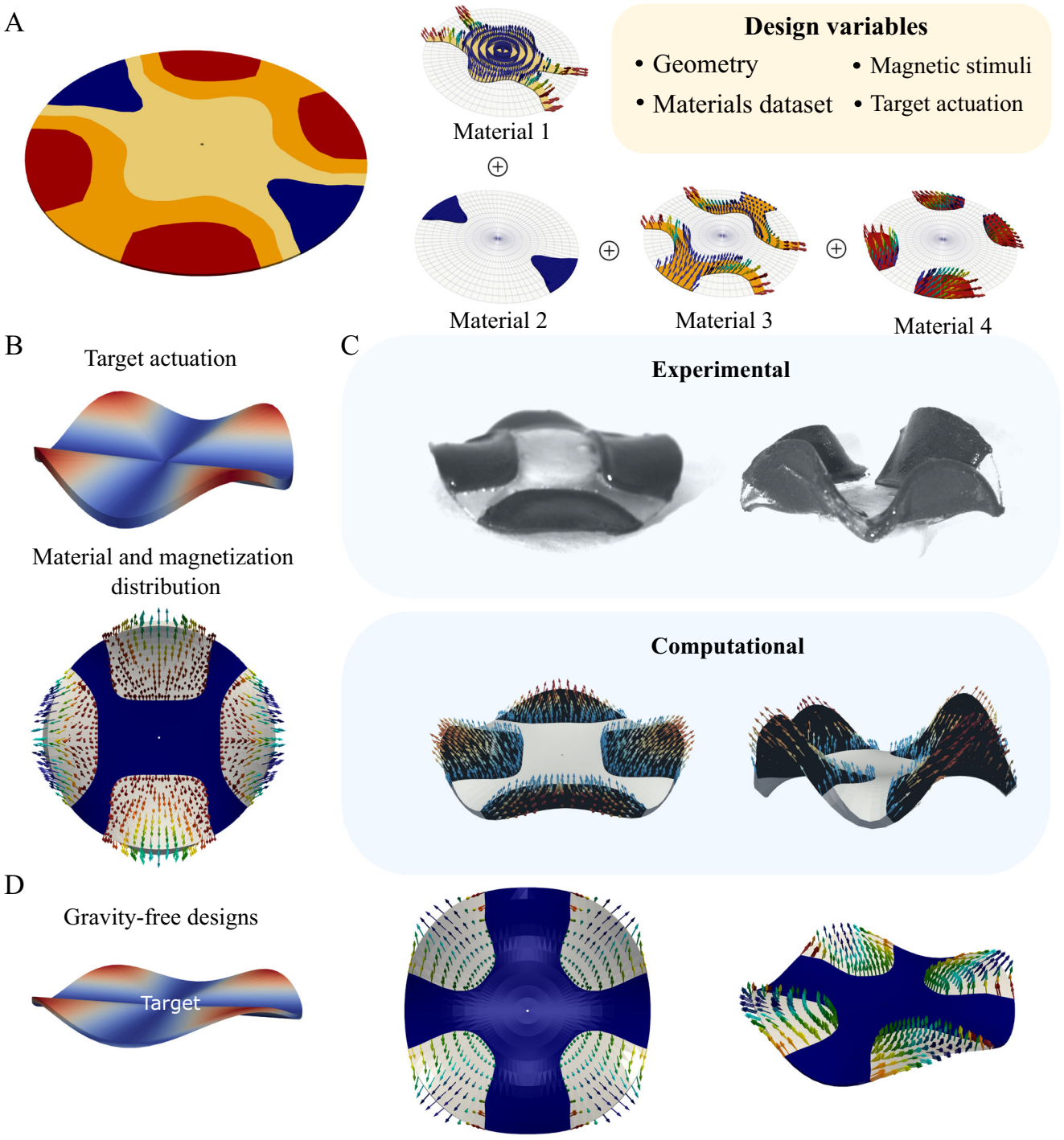

Figure 5. Multimaterial optimization and experimental validation of programmable hMRE actuators. A) Schematic representation of the design workflow. Given a set of calibrated constitutive models (e.g., passive and magneto-active elastomers), a target actuation, and a defined geometry, the framework simultaneously optimizes the spatial distribution of materials and the residual magnetization field across the domain. B) Target deformation (top) and optimized design (bottom), showing the spatial layout of materials and the corresponding residual magnetization vectors. C) Comparison between experimental (top) and computational (bottom) actuation responses for the optimized design in B, validating the predictive power of the framework. D) Gravity-free version of the design problem shown in (B), simulating an underwater-like scenario by neglecting gravitational forces. The resulting distribution and deformation highlight the impact of gravity on ultra-soft magneto-active systems. A distinct optimal distribution of both materials and residual magnetization emerges when gravitational forces are neglected, in contrast to the design obtained under gravity in (B).

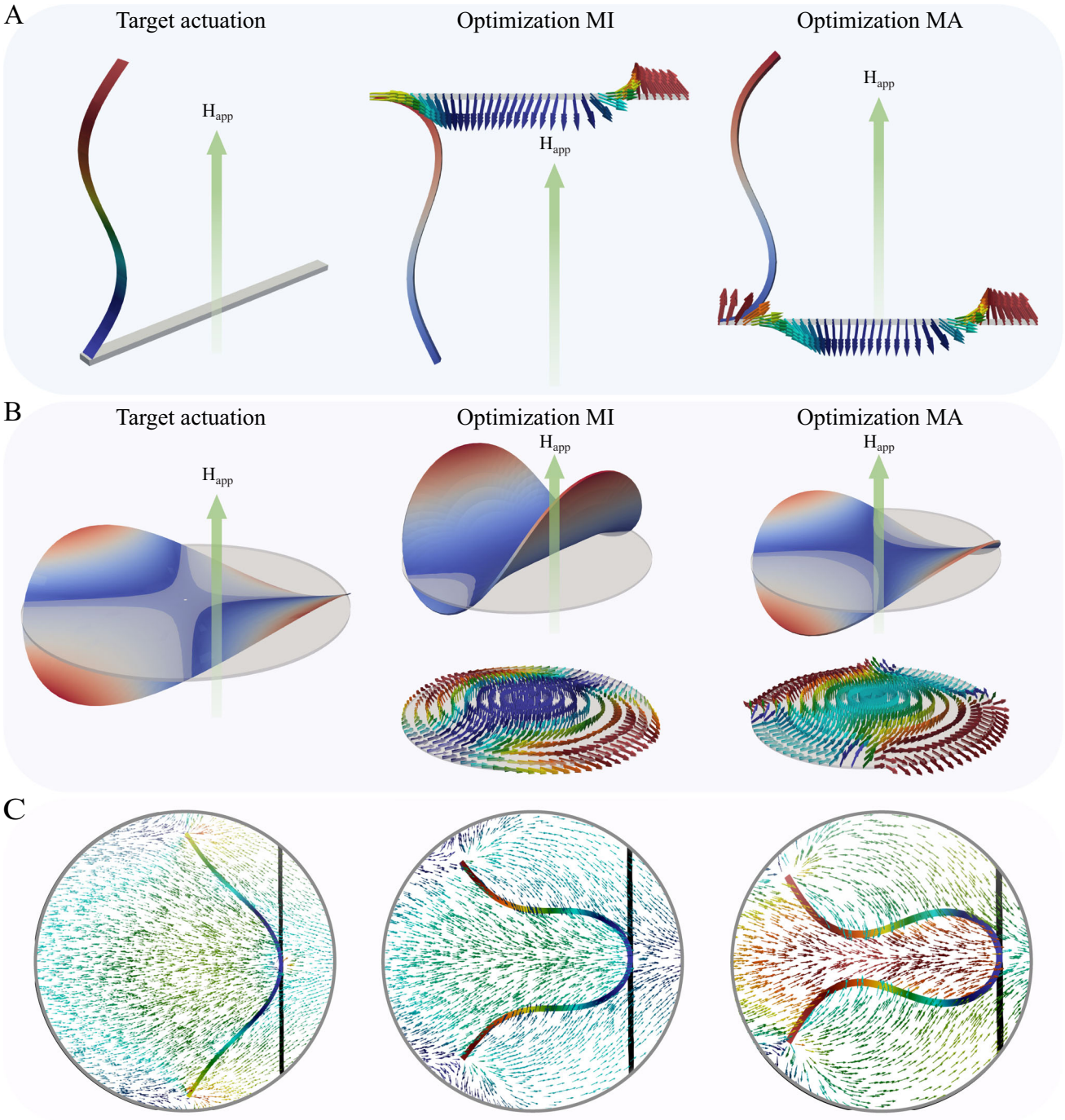

Figure 6. Impact of magnetic remanence-induced anisotropy on inverse design strategies in ultra-soft hMREs. A) Inverse design of a beam-shaped actuator. The left panel shows the target deformation under an applied magnetic field $\mathbf{H}_{app}$. The middle and right panels show the residual magnetization distribution and resulting deformation obtained via topology optimization excluding (MI model) and including (MA model) the effects of magnetic anisotropy. Neglecting anisotropy leads to significant deviation from the target shape. B) Inverse design of a shell-like actuator. The same comparison between target actuation (left), MI-based optimization (middle), and MA-based optimization (right) is shown. Ignoring anisotropy results in a completely different actuation mode. C) Magneto-mechanical simulation of a beam actuator, including vacuum–solid magnetic interactions. The figure shows the deformed configuration and the magnetic field lines in the surrounding space. These results highlight the importance of solving the full magneto-mechanical problem to capture long-range interactions in soft hMRE systems.

accurate actuation performance. It is important to note that all formulations and simulations can be implemented and solved in a fully 3D framework, even when the validation examples correspond to beam- or shell-like structures. These configurations are chosen not as simplifications, but because they represent the most effective typologies to exploit the large-deformation and anisotropic actuation mechanisms that characterize ultra-soft hMREs.

Figure 6C further highlights the importance of considering the full magneto-mechanical coupling (see Figure S12, Supporting Information). Here, we simulate the actuation of a soft hMRE structure composed of multiple magnetized regions in close proximity. The results show that the deformation of each region is not independent, but strongly influenced by the magnetic field generated by the others. This interdependence arises from magnetic interactions in the surrounding vacuum and leads to collective effects that cannot be captured by simplified, decoupled models. Only a complete field-based solution, accounting for the interactions between domains, can reproduce the observed behavior. The importance of explicitly solving the magnetic field in both the solid and the surrounding air is further illustrated in the Supporting Information (Figure S13, Supporting Information), where a comparison between homogeneous-field and permanent-magnet actuation highlights the strong influence of field heterogeneity on the resulting deformation. These findings underscore the necessity of modeling not only the anisotropic response of the material but also the magnetic interactions between spatially distributed active regions when designing hMRE structures.

Overall, this final set of examples reinforces the importance of incorporating full-physics models, including remanent-field-driven anisotropy and long-range magnetic coupling, into inverse design frameworks for ultra-soft magneto-active systems. Failure to do so can lead to incorrect predictions, mode switching, and ultimately ineffective or nonfunctional designs.

3. Discussion

In this work, we have introduced a comprehensive experimental and computational framework to characterize, model, and design ultra-soft hard-magnetic elastomers (hMREs) with programmable magneto-mechanical actuation. Our results show that residual magnetization in these materials induces a persistent mechanical anisotropy, even in the absence of applied fields. Although this effect is neglected in existing models and design strategies, we demonstrate both experimentally and computationally that such anisotropy can significantly alter the mechanical response, not only in magnitude, but also in the qualitative deformation modes. This insight is captured through an invariant-based, polyconvex neural network constitutive model, which enables the robust simulation of anisotropic behavior and its integration into topology and multi-material optimization platforms. Our findings go beyond conventional approaches by introducing physical consistency and constitutive generality into the design loop, showing that accurate modeling of remanence-induced anisotropy is critical for the predictive design of soft magnetically actuated systems, particularly in the ultra-soft regime.

A key observation from our experiments is that, under strong magnetic fields, ultra-soft hMREs like those based on Dowsil matrices can undergo deformation patterns that deviate from typical structural actuation. As the field intensity increases, magnetic torques on the embedded particles dominate over the elastic restoring forces of the matrix. This leads to localized torsion or particle-driven rotations, effectively introducing new deformation mechanisms that are not captured by standard continuum assumptions. Although the present framework operates at the continuum scale, establishing a quantitative micro–macro correlation for these effects would require dedicated multiscale or micromorphic formulations capable of resolving particle reorientation and internal rotational degrees of freedom. Such developments fall beyond the scope of this work but represent a promising direction for future research.

It is also important to note that the full modeling and optimization framework presented here was developed and validated using hMREs composed of Nd-based microparticles. These particles exhibit high magnetic remanence but very low magnetic susceptibility,[41] which in many scenarios allows simplifying the simulation of magnetic fields by decoupling the material response from its interaction with the surrounding vacuum.[6,51,52] However, this assumption breaks down when the hMRE structure deforms in such a way that different spatial domains come into close proximity, leading to significant magnetic interactions between them.[15] Moreover, solving the full problem, including the vacuum domain, becomes essential when dealing with materials exhibiting higher magnetic susceptibility, even in the absence of large deformations.[44,53] For instance, recent developments have introduced hybrid MREs that combine hard- and soft-magnetic particles, yielding materials with both high remanence and enhanced susceptibility.[54] In such cases, the mutual magnetic influence between different regions of the structure, especially through the vacuum, becomes non-negligible. This is illustrated in Figure 6C, where even in low-χ materials, spatial proximity between magnetized regions leads to cross-domain magnetic interactions that significantly affect deformation. For higher-χ materials, these effects are stronger, and require full magnetostatic formulations including vacuum effects to achieve accurate simulations and designs (see Figure S14, Supporting Information).

More broadly, a critical implication of our findings is that these anisotropic and remanence-driven effects can trigger bifurcations or mechanical instabilities, shifting the system from one deformation mode to another. This is especially important in the design of compliant morphing systems and soft actuators, where small changes in stiffness or directional reinforcement can lead to qualitative shifts in mechanical behavior. Our results show that ignoring remanence-induced anisotropy does not merely reduce accuracy, it can completely mislead the design, resulting in the emergence of unintended or even counterproductive actuation patterns. This underscores the need for constitutive and numerical models that are not only robust and efficient, but also physically accurate and aware of the dominant mechanisms at play.

Together, these observations reveal that the magneto-mechanical behavior of ultra-soft hMREs is far richer than previously assumed, with a wide spectrum of coupled effects that must be considered for rational design. Although our framework marks a significant step forward in modeling and programming these materials, it also opens the door to further investigations into microstructural dynamics, vacuum coupling,

and critical phenomena in magnetically responsive soft matter.

4. Experimental Section

Material and Manufacturing Methods for Material Characterization Specimens: For the mechanical characterization experiments, samples with dimensions of 40 mm length, 5 mm width, and 3 mm thickness were fabricated using ABS molds. ABS was selected due to its dimensional stability and thermal resistance under the curing conditions used, and the molds were 3D-printed using an Original Prusa XL printer (Prusa Research, Czech Republic). The samples were prepared using either virgin PDMS or PDMS mixed with hard-magnetic particles. Two types of PDMS were employed: Dowsil CY52-276 (DowSil, Midland, MI, USA) and Sylgard 184 (Dow Corporate, MI, USA), used in separate batches. For the magnetic composites, neodymium-iron-boron (NdFeB) powder (grade MQP-S-11-9, Neo Materials Technology Inc., Greenwood Village, CO, USA) was added to the PDMS matrix at volume fractions of 20%, 30%, and 40%. In the case of Dowsil-based samples, the two liquid components were mixed in a 1:1 ratio to initiate the crosslinking reaction, both for the virgin PDMS and for the hMREs containing magnetic particles. To ensure homogeneous particle distribution and prevent sedimentation, the hMRE mixture was degassed and preheated to 80 °C for 1.5 min to increase its viscosity before pouring. The preheated mixture was then cast into molds that had also been preheated to 80 °C to avoid disrupting the crosslinking kinetics, and cured at the same temperature for 3 h in an oven. Sylgard 184-based samples were processed following the same procedure, except that the two PDMS components were mixed at a 10:1 ratio, as per manufacturer recommendations.

After curing, the elastomeric samples were demolded and transferred to custom 3D-printed molds fabricated in Durable V2 resin using a Form 3+ printer (Formlabs Inc., USA). These molds were designed to impose specific pre-magnetization orientations of 0°, 45°, and 90° relative to the longitudinal axis of the sample. Pre-magnetization was performed by applying a uniform magnetic pulse of 3 T using an impulse magnetizer (DXMM-12C40, DexingMagnet Tech. Co., Ltd., China), ensuring full saturation of the embedded magnetic particles. The impulse magnetization process consisted of a single, short-duration pulse (a few ms), which did not produce any measurable heating in the samples; temperature monitoring before and after magnetization confirmed variations below the instrument resolution, ensuring that no thermal effects influence the material properties.

Materials and Manufacturing Methods for c-shaped hMREs Samples: These specimens were fabricated using Dowsil CY52-276 and Sylgard 184, employing the same mixing ratios and fabrication process as in the mechanical characterization tests. The only difference was in the geometry of the mold, which in this case had dimensions of 100 mm length, 5 mm width, and 2 mm thickness. After curing, the samples were placed into a ring-shaped mold designed to impose a curved pre-magnetization configuration. This secondary mold had an inner radius of 20 mm and a thickness of 2 mm. It included an open top section, whose arc length matched the length of the specimen, enabling the sample to adopt the curved shape during pre-magnetization. A 3 T magnetic field was then applied using an impulse magnetizer (DXMM-12C40, DexingMagnet Tech. Co., Ltd., China) to magnetize the specimen in the deformed state. The curved mold was cast from Elite Double 32 silicone rubber using a 1:1 mixing ratio and cured at room temperature for 20 min. To form the internal cavity, the silicone was poured over an ABS mould that had been 3D-printed on an Original Prusa XL printer, reproducing the desired ring geometry.

Materials and Manufacturing Methods for 2D Circular-Shaped hMREs Samples: Two types of molds were 3D-printed in ABS using an Original Prusa XL printer for the fabrication of these samples. The first mold consisted of a square frame with a cavity coinciding with the magnetoactive domains, whose geometry was directly exported from the numerical model as an stl file. The second mold corresponded to the deformed configuration with the local residual magnetizations aligned vertically with the impulse magnetic field, and was used to impose the magnetization orientation during pre-magnetization.

For the ultra-soft materials fabrication, the first mold was first filled with the PDMS matrix mixed with NdFeB particles at the desired concentration. To prevent sedimentation, the mixture was degassed and preheated in the oven at 80 °C for 1.5 min prior to casting, and then cured at the same temperature for 3 h. After curing, the magnetic subdomains were demolded and placed into the second (pre-magnetization) mold, where a magnetic field of 3 T was applied using the impulse magnetizer to align the residual magnetization according to the imposed deformation. Once magnetized, the magnetic components were repositioned into their original locations within the square mold. Finally, the virgin PDMS matrix was poured into the remaining voids to complete the sample, followed by a final curing step of 2 h at 80 °C.

Experimental Procedure for hMREs Mechanical Anisotropy Characterization: For these tests, a universal testing machine (INSTRON 34TM-5, Instron, MA, USA) was employed, equipped with a 50 N load cell and INSTRON pneumatic grips for samples based on the Dowsil matrix, and with a 5 kN load cell and INSTRON mechanical grips for specimens based on the Sylgard matrix. The samples were tested under uniaxial quasi-static conditions with an initial gauge length of 25 mm and a strain rate of $\dot{\epsilon} = 0.001\,\mathrm{s}^{-1}$. For both elastomeric matrices, each test was performed on three different specimens for each combination of Nd particle concentration (0%, 20%, 30%, and 40%) and magnetization orientation relative to the longitudinal axis of the specimen (0°, 45°, and 90°).

Experimental Procedure for hMREs Actuation Under a Homogeneous External Magnetic Field: The samples were placed inside a Helmholtz coil (Dexin Mag), capable of generating a uniform magnetic field of up to 50 mT within a cubic volume of 15 × 15 × 15 cm^3. For 1D geometries, the specimens were positioned on a horizontal surface previously lubricated with WD-40 oil (WD-40 Company Limited, Madrid, Spain) to prevent adhesion during testing. For 2D samples, a concentric circular support was employed to reproduce the boundary conditions defined in the numerical simulations. Once the specimens were properly positioned, the magnetic field was applied using a ramp of ≈0.8 mT until reaching the maximum field strength, H_{max}.

Neural Network-Based Constitutive Modeling: The magneto-mechanical behavior of hMREs is governed by strong nonlinear couplings between deformation, internal anisotropy, and remanent magnetic fields. Capturing these effects required constitutive models that go beyond traditional phenomenological formulations. To this end, a neural network (NN)-based framework was adopted that mapped a set of invariants to the scalar energy density Ψ, as introduced in Results section.

The energy density was expressed as a function of a set of magneto-mechanical invariants $\{I_1, I_2, I_3, I_4, I_5, I_5^{er}, I_6\}$, and learned from experimental data through a neural network model:

$$\Psi(\mathbf{F}, \mathbf{H}, \mathcal{W}) = \mathbb{U}(I_1, I_2, I_3, I_4, I_5, I_5^{er}, I_6; \mathcal{W}) \tag{3}$$

where $\mathcal{W}$ denotes the set of weights and biases of the neural network:

$$\mathcal{W} = \{\mathbf{W}_1, \ldots, \mathbf{W}_{L+1}, \mathbf{b}_1, \ldots, \mathbf{b}_{L+1}\} \tag{4}$$

The NN is trained using a Sobolev-type loss function that minimizes the discrepancy between predicted and measured first-order derivatives (i.e., stresses) for the case $\mathbf{H} = \mathbf{0}$:[53]

$$\mathcal{L}(\mathcal{W}) = \frac{\sum_{i=1}^{n_d} \left\| \mathbf{P}^i - \partial_{\mathbf{F}} \Psi(\mathbf{F}^i, \mathbf{0}, \mathcal{W}) \right\|^2}{\sum_{i=1}^{n_d} \left\| \mathbf{P}^i \right\|^2} \tag{5}$$

where n_d is the number of training samples, and $\mathbf{P}^i$ are the experimentally measured first Piola–Kirchhoff stresses. This Sobolev training approach improves generalization and ensures physically meaningful gradients across the deformation space (see Supporting Information).

To ensure numerical stability and physical consistency, the network was designed to satisfy polyconvexity[55–57] by construction. This was achieved

by expressing the energy in terms of the deformation gradient **F**, its cofactor Cof**F**, its determinant J, and the magnetic field **H**:

$$\Psi(\mathbf{F}, \mathbf{H}, \mathcal{W}) = \mathbb{W}(\mathbf{F}, \mathrm{Cof}\,\mathbf{F}, J, \mathbf{H}, \mathcal{W}) \tag{6}$$

where $\mathbb{W}$ is a convex function with respect to the three first arguments, namely, with respect to $\boldsymbol{F}$, $\boldsymbol{H}$, and J. Polyconvexity was promoted through architectural constraints: non-negative weights and monotonically increasing activation functions (e.g., SoftPlus), and enforced during training via the penalty term:

$$\widetilde{\mathcal{L}}(\mathcal{W}) = \mathcal{L}(\mathcal{W}) + \frac{\kappa_r}{2} \sum_i (\min((\mathcal{W}_v)_i, 0))^2 \tag{7}$$

where $\mathcal{W}_v$ is the concatenated vector of all weights subject to positivity, and κ_r is a regularization parameter. Full implementation details are provided in the Supporting Information.

Additionally, to enforce that the undeformed configuration is stress-free, a regularization loss was added that penalized residual forces at $\mathbf{F} = \mathbf{I}$ and $\mathbf{H} = \mathbf{0}$. This constraint ensured compatibility with experimental reference states and enhanced robustness during inverse design (see Supporting Information).

Finite Element Implementation: The numerical resolution of the coupled magneto-mechanical problem was performed via a custom finite element implementation using a staggered scheme. The formulation was based on the balance equations for linear momentum and magnetostatics, expressed in strong form. All numerical experiments were performed using the Julia programming language, leveraging the Gridap framework[58] for the approximation of partial differential equations (PDEs) and the HyperFEM module [https://github.com/MultiSimOLab/HyperFEM] for modeling nonlinear physical problems in multifunctional materials.

Governing equations. The mechanical problem was governed by the balance of linear momentum in the absence of body forces:

$$\mathrm{Div}\,\mathbf{P} = \mathbf{0} \quad \text{in } \Omega_0 \tag{8}$$

where **P** is the first Piola–Kirchhoff stress tensor and Ω_0 is the reference configuration. The magnetic problem was governed by the magnetostatic Maxwell equations:

$$\mathrm{Curl}\,\mathbf{H} = \mathbf{0} \quad \text{in } \Omega_0 \tag{9}$$

$$\mathrm{Div}\,\mathbf{B} = 0 \quad \text{in } \Omega_0 \tag{10}$$

Full definitions of the variables are provided in the Supporting Information.

Numerical solution via staggered scheme. The magneto-mechanical problem was solved using a staggered approach that decouples the magnetic and mechanical fields, as outlined in the Supporting Information (Algorithm 1). Each iteration consisted of the following steps:

a) **Step 1: Magnetostatic subproblem**. The scalar magnetic potential φ was computed by solving Equation (5) in the entire domain (hMRE and vacuum). Continuity and boundary conditions were imposed across interfaces and on the boundary.
b) **Step 2: Mechanical subproblem in the solid**. The deformation mapping $\boldsymbol{\phi}$ was computed in the solid domain Ω_0 by solving the equilibrium equation $\mathrm{Div}\,\mathbf{P} = \mathbf{f}_0$. Dirichlet and Neumann boundary conditions were applied as appropriate, and **H** is taken from Step 1.
c) **Step 3: Mechanical subproblem in the surrounding vacuum**. A linear elastic problem was solved in the vacuum region Ω_{v0} using a potential $\boldsymbol{\phi}_v$, enforcing continuity with the solid deformation and applying clamped boundary conditions on its boundary.
d) **Step 4: Update and convergence check**. Convergence was assessed based on changes in displacement fields in both domains. If the Jacobian $J = det(\mathbf{F})$ becomes negative or extreme distortions are detected, the mesh is refined or penalization exponents are adjusted.

This iterative strategy ensured stability in the presence of strong magneto-mechanical coupling, especially under large deformations. Full implementation details are provided in the Supporting Information.

Simplified formulation. In cases involving magnetic fillers with very low susceptibility (e.g., $\chi \approx 0$), the magnetic permeability of the material was close to that of vacuum. This allowed for a simplified approximation where the magnetic field was assumed to be unaffected by the deformation, i.e., $\mathbf{H} \approx \mathbf{H}_{\mathrm{app}}$. This assumption decoupled the magnetic field solution from the mechanical problem and avoided the need to solve Equation (4) altogether. In this case, the magnetic response was entirely encoded through the residual field and the magneto-mechanical response can be evaluated by directly inserting $\mathbf{H}_{\mathrm{app}}$ into the constitutive model. This simplification significantly reduced computational cost and remained accurate for materials with negligible magnetization-induced fields. A complete discussion and validation of this approach is provided in the Supporting Information.

Optimization Framework: To design programmable magneto-mechanical responses, a topology and multimaterial optimization problem was formulated, where the goal was to determine the spatial distribution of materials, residual magnetization vectors, and actuation parameters that minimized a prescribed objective functional under the coupled magneto-mechanical behavior of the system. Within this framework, the residual magnetic field $\mathbf{H}_r$ was defined in spherical coordinates as:

$$\mathbf{H}_r = H_r \mathbf{N}(\theta, \varphi), \quad \mathbf{N}(\theta, \varphi) = \left[\cos(\theta)\sin(\varphi)\ \ \sin(\theta)\sin(\varphi)\ \ \cos(\varphi)\right] \tag{11}$$

where H_r is the residual magnetization determined by the particles' content, and (θ, φ) are the angular degrees of freedom used as design variables. The applied magnetic field $\mathbf{H}_{\mathrm{app}}$ is assumed to have a fixed direction $\mathbf{N}_{H_a}$, such that $\mathbf{H}_{\mathrm{app}} = H_{\mathrm{app}}\mathbf{N}_{H_a}$.

Material interpolation is performed through a density field $\xi: \Omega_0 \to [0, 1]$, where $\xi = 0$ indicates passive regions and $\xi = 1$ corresponds to magnetically active ones. The total energy density is then defined as:

$$\Psi(\xi, c, \theta, \varphi, H_{\mathrm{app}}, \mathbf{F}) = (1 - \xi^{p_\xi})\Psi_p(\mathbf{F}) + \xi^{p_\xi}\Psi_a(c, \theta, \varphi, H_{\mathrm{app}}, \mathbf{F}) \tag{12}$$

where p_ξ is a penalization parameter, and Ψ_p, Ψ_a denote the strain energy densities of the passive and active phases, respectively.

Numerical Resolution Method: A gradient-based optimization scheme was adopted, where the descent directions for all design variables $(\xi, c, \theta, \varphi, H_{\mathrm{app}})$ were computed through an adjoint-based formulation. The optimization problem was solved by minimizing an objective functional $\mathcal{J}(\phi)$, which was enforced via the Lagrangian:

$$\mathcal{L}(\phi, \mathbf{p}, \xi, c, \theta, \psi, H_{\mathrm{app}}) = \mathcal{J}(\phi) - \left(\int_{\Omega_0} \mathbf{P}(\xi, c, \theta, \psi, H_{\mathrm{app}}, \nabla_0\phi) : \nabla_0\mathbf{p}\, dV - \int_{\Omega_0} \mathbf{f}_0 \cdot \mathbf{p}\, dV \right) \tag{13}$$

where **p** is the adjoint variable. The optimization proceeds as follows: The optimization procedure follows a standard gradient-based approach, where the design variables $(\xi, c, \theta, \psi, H_{\mathrm{app}})$ were iteratively updated to minimize the objective functional. Each optimization iteration proceeds through the following steps:

1) **Solve the forward (state) problem**: Given the current design variables, the magneto-mechanical equilibrium equations were solved to compute the deformed configuration ϕ and the associated fields.
2) **Solve the adjoint problem**: The adjoint field **p** was obtained by solving the variational adjoint equations associated with the Lagrangian functional.
3) **Evaluate the objective functional**: The current value of the objective $\mathcal{J}(\xi, c, \theta, \psi, H_{\mathrm{app}})$ was computed.

4) **Compute sensitivities**: The descent directions were computed by evaluating the derivatives of the Lagrangian $\mathcal{L}$ with respect to all design variables:

$$\nabla\mathcal{L} = \left(\partial_{\xi}\mathcal{L},\ \partial_{c}\mathcal{L},\ \partial_{\theta}\mathcal{L},\ \partial_{\psi}\mathcal{L},\ \partial_{H_{\text{app}}}\mathcal{L}\right) \tag{14}$$

5) **Update step**: A suitable step size Δ was determined (e.g., via line search), and the design variables were updated as:

$$(\xi, c, \theta, \psi, H_{\text{app}}) \leftarrow (\xi, c, \theta, \psi, H_{\text{app}}) + \Delta \tag{15}$$

6) **Convergence check**: The process was repeated until the change in the design variables or objective value fell below a prescribed threshold.

This framework enabled simultaneous optimization of material layout, magnetic programming, and actuation inputs. Full derivations, sensitivity expressions, and implementation details are provided in the Supporting Information.

Supporting Information

Supporting Information is available from the Wiley Online Library or from the author.

Acknowledgements

C.P.Z. and R.O. contributed equally to this work. The authors acknowledge technical support by Maria Luisa Lopez-Donaire and Maria Fernanda Betancourt-Soto. The authors acknowledge support from the European Research Council (ERC) under the European Union's Horizon 2020 Research and Innovation Program (grant agreement no. 947723, project: 4D-BIOMAP, and grant agreement no. 101247449, project: MAGMATED), and Sponsorship agreement UC3M-NAVANTIA-MONODON. R. Ortigosa and J. Martínez-Frutos acknowledge the support of grant PID2022-141957OA-C22 funded by MICIU/AEI/10.13039/501100011033 and by "ERDF A way of making Europe". They also acknowledge the support provided by the Autonomous Community of the Region of Murcia, Spain, through the programme for the development of scientific and technical research by competitive groups (21996/PI/22), included in the Regional Program for the Promotion of Scientific and Technical Research of Fundación Séneca-Agencia de Ciencia y Tecnología de la Región de Murcia. Funding for APC: Universidad Carlos III de Madrid (Agreement CRUE-Madroño 2025).

Conflict of Interest

The authors declare no conflict of interest.

Data Availability Statement

The data that support the findings of this study are available from the corresponding author upon reasonable request. Some examples of the codes developed in this study are available in https://github.com/MultiSimOLab/Adv_Mater_Ultra_Soft_Magnet.

Keywords

magneto-mechanics, magnetorheological elastomers, multifunctional materials, soft robotics, topology optimization

Received: September 19, 2025
Revised: October 31, 2025
Published online:

[1] Q. Chen, T. Kalpoe, J. Jovaa, *Heliyon* **2024**, *10*, e34026.
[2] R. Ma, L. Wu, D. Pasini, *Adv. Funct. Mater.* **2023**, *33*, 2213371.
[3] Z. Wang, J. Wang, J. Ayarza, T. Steeves, Z. Hu, S. Manna, A. P. Esser-Kahn, *Nat. Mater.* **2021**, *20*, 869.
[4] Z. Zhao, S. Chen, P. Zhao, W. Luo, Y. Luo, J. Zuo, C. Li, *Angew. Chem. Int. Ed.* **2024**, *63*, e202400758.
[5] C. Perez-Garcia, J. Aranda-Ruiz, M. L. Lopez-Donaire, R. Zaera, D. Garcia-Gonzalez, *Adv. Funct. Mater.* **2024**, *34*, 2313865.
[6] C. Wang, Z. Zhao, J. Han, A. A. Sharma, H. Wang, X. S. Zhang, *Adv. Sci.* **2024**, *11*, 2308619.
[7] H. Lou, Y. Wang, Y. Sheng, H. Zhu, S. Zhu, J. Yu, Q. Zhang, *Adv. Sci.* **2024**, 2405021.
[8] F. Niu, Q. Xue, Q. Cao, X. He, T. Wang, H. Wang, C. Hao, X. Li, Y. Li, H. Yang, H. Yang, D. Han, *Int. J. Extrem. Manuf.* **2025**, *7*, 055506.
[9] Y. Kim, G. A. Parada, S. Liu, X. Zhao, *Sci. Robot.* **2019**, *4*, eaax7329.
[10] A. Tay, A. Sohrabi, K. Poole, S. Seidlits, D. Di Carlo, *Adv. Mater.* **2018**, *30*, 1800927.
[11] C. Gomez-Cruz, M. Fernandez-de La Torre, D. Lachowski, M. Prados-de-Haro, A. E. Del Río Hernández, G. Perea, A. Muñoz-Barrutia, D. Garcia-Gonzalez, *Adv. Mater.* **2024**, *36*, 2312497.
[12] C. Fang, B. Xu, M. Li, J. Han, Y. Yang, X. Liu, *Adv. Fiber Mater.* **2024**, *6*, 622.
[13] K. Wu, W. He, R. Zhong, Z. Nie, X. Lin, M. Han, *Mater. Horiz.* **2025**, *12*, 7192.
[14] S. Yi, L. Wang, Z. Chen, J. Wang, X. Song, P. Liu, Y. Zhang, Q. Luo, L. Peng, Z. Wu, C. F. Guo, L. Jiang, *Nat. Commun.* **2022**, *13*, 4177.
[15] C. Perez-Garcia, R. Zaera, J. Aranda-Ruiz, G. Bordiga, G. Risso, M. L. Lopez-Donaire, K. Bertoldi, D. Garcia-Gonzalez, *Adv. Mater.* **2025**, *37*, 2412353.
[16] A. Rossi, F. Furlani, G. Bassi, C. Cunha, A. Lunghi, F. Molinari, F. J. Teran, F. Lista, M. Bianchi, A. Piperno, M. Montesi, S. Panseri, *Mater. Today Bio* **2024**, *27*, 101110.
[17] A. López-Díaz, A. S. Vázquez, E. Vázquez, *ACS Nano* **2024**, *18*, 20817.
[18] Q. Ze, S. Wu, J. Dai, S. Leanza, G. Ikeda, P. C. Yang, G. Iaccarino, R. R. Zhao, *Nat. Commun.* **2022**, *13*, 3118.
[19] M. A. Moreno-Mateos, K. Danas, D. Garcia-Gonzalez, *Mech. Mater.* **2023**, *184*, 104742.
[20] K. Danas, M. Nakano, G. Sebald, *Mech. Mater.* **2025**, *200*, 105187.
[21] D. Yan, M. Pezzulla, L. Cruveiller, A. Abbasi, P. M. Reis, *Nat. Commun.* **2021**, *12*, 2831.
[22] E. Gonzalez-Saiz, M. L. Lopez-Donaire, L. Gutiérrez, K. Danas, D. Garcia-Gonzalez, *Adv. Sci.* **2025**, e06790.
[23] A. K. Bastola, M. Hossain, *Compos. Part B Eng.* **2020**, *200*, 108348.
[24] R. Zabihyan, J. Mergheim, J. Pelteret, B. Brands, P. Steinmann, *Int. J. Solids Struct.* **2020**, *193-194*, 338.
[25] J. Gonzalez-Rico, S. Garzon-Hernandez, C. M. Landis, D. Garcia-Gonzalez, *J. Mech. Phys. Solids* **2024**, *192*, 105791.
[26] M. Li, A. Pal, J. Byun, G. Gardi, M. Sitti, *Adv. Mater.* **2023**, *35*, 2304825.
[27] Q. Zhang, A. V. Cherkasov, C. Xie, N. Arora, S. Rudykh, *Int. J. Solids Struct.* **2023**, *280*, 112396.
[28] M. Moreno, J. Gonzalez-Rico, M. Lopez-Donaire, A. Arias, D. Garcia-Gonzalez, *Compos. Part B Eng.* **2021**, *224*, 109148.
[29] A. Dargahi, R. Sedaghati, S. Rakheja, *Compos. Part B Eng.* **2019**, *159*, 269.
[30] E. Yildiz, U. Bozuyuk, E. Yildiz, F. Wang, M. Han, A. C. Karacakol, D. Sheehan, Y. Yu, M. Sitti, *Adv. Sci.* **2025**, *12*, https://doi.org/10.1002/advs.202507569.
[31] Z. Li, Y. Wang, Z. Wang, C. Kadapa, M. Hossain, X. Yao, J. Wang, *J. Mech. Phys. Solids* **2025**, *200*, 106089.
[32] Z. Lin, Z. Hooshmand-Ahoor, L. Bodelot, K. Danas, *J. Mech. Phys. Solids* **2025**, *203*, 106218.
[33] K. A. Kalina, A. Rassloff, M. Wollner, P. Metsch, J. Brummund, M. Kästner, *Phys. Sci. Rev.* **2023**, *8*, 1.

[34] Y. Kim, H. Yuk, R. Zhao, S. A. Chester, X. Zhao, *Nature* **2018**, *558*, 274.
[35] A. F. Sukarman, S. Mohd Yusuf, S. A. Mazlan, N. A. Nordin, D. M. Patel, M. A. F. Johari, N. H. Lazim, K. A. A. Kadir, *Polym. Eng. Sci.* **2025**, *65*, 1977.
[36] G. Z. Lum, Z. Ye, X. Dong, H. Marvi, O. Erin, W. Hu, M. Sitti, *Proc. Natl. Acad. Sci. U.S.A.* **2016**, *113*, 41.
[37] A. Bastola, L. Parry, R. Worsley, N. Ahmed, E. Lester, R. Hague, C. Tuck, *Addit. Manuf. Lett.* **2024**, *11*, 100250.
[38] H. Wu, Z. Xu, J. Wang, X. Bo, Z. Tang, S. Jiang, G. Zhang, *J. Magn. Magn. Mater.* **2021**, *527*, 167693.
[39] S. Mahle, P. Ilg, M. Liu, *Phys. Rev. E* **2008**, *77*, 016305.
[40] M. A. Moreno-Mateos, M. L. Lopez-Donaire, M. Hossain, D. Garcia-Gonzalez, *Smart Mater. Struct.* **2022**, *31*, 065018.
[41] R. Zhao, Y. Kim, S. A. Chester, P. Sharma, X. Zhao, *J. Mech. Phys. Solids* **2019**, *124*, 244.
[42] Q. Ze, X. Kuang, S. Wu, J. Wong, S. M. Montgomery, R. Zhang, J. M. Kovitz, F. Yang, H. J. Qi, R. Zhao, *Adv. Mater.* **2020**, *32*, 1906657.
[43] J. Zhang, L. Zhu, X. Guo, Y. Qiao, M. Zhang, P. Zhai, *J. Magn. Magn. Mater.* **2024**, *604*, 172291.
[44] E. M. Stewart, L. Anand, *J. Mech. Phys. Solids* **2025**, *194*, 105934.
[45] D. Mukherjee, M. Rambausek, K. Danas, *J. Mech. Phys. Solids* **2021**, *151*, 104361.
[46] D. Mukherjee, K. Danas, *Int. J. Solids Struct.* **2022**, *257*, 111513.
[47] K. Danas, P. M. Reis, *J. Mech. Phys. Solids* **2024**, *191*, 105764.
[48] N. Xia, D. Jin, C. Pan, J. Zhang, Z. Yang, L. Su, J. Zhao, L. Wang, L. Zhang, *Nat. Commun.* **2022**, *13*, 7514.
[49] R. J. Williams, C. M. Davies, P. A. Hooper, *Addit. Manuf.* **2018**, *22*, 416.
[50] G. A. Holzapfel, R. W. Ogden, *Eur. J. Mech. A/Solids* **2025**, *112*, 105634.
[51] Z. Zhao, X. S. Zhang, *J. Mech. Phys. Solids* **2022**, *158*, 104628.
[52] L. Wang, *Comput. Methods Appl. Mech. Eng* **2025**, *445*, 118205.
[53] M. Rambausek, D. Mukherjee, K. Danas, *Comput. Methods Appl. Mech. Eng* **2022**, *391*, 114500.
[54] M. A. Moreno-Mateos, M. Hossain, P. Steinmann, D. Garcia-Gonzalez, *npj Comput. Mater.* **2022**, *8*, 162.
[55] J. M. Ball, *Arch. Ration. Mech. Anal.* **1976**, *63*, 337.
[56] J. M. Ball, *Geometry, Mechanics and Dynamics*, Springer, Berlin **2002**.
[57] J. Schröder, P. Neff, D. Balzani, *Int. J. Solids Struct.* **2005**, *42*, 4352.
[58] S. Badia, F. Verdugo, *J. Open Source Softw.* **2020**, *5*, 2520.